1

1
Observational Details: Radio
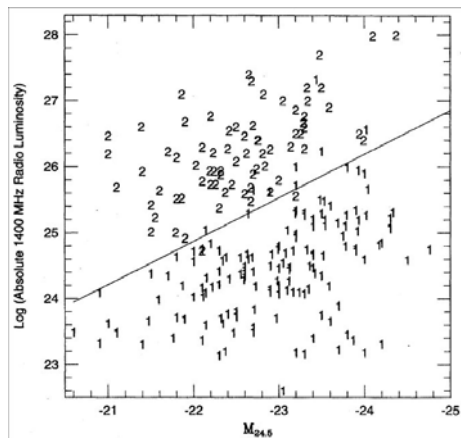
A.H.Bridle & M.H.Cohen

1.1
Overall structures of radio sources

Figure 1.1 Fanaroff-Riley morphological classification vs. radio and optical luminosities, from Ledlow & Owen (1996). FR I sources are plotted with symbol '1', FR II sources with symbol '2'. Reproduced by permission of the American Astronomical Society.

In this chapter we discuss the observations of radio jets. After some introductory remarks, mainly describing the classic Fanaroff-Riley separation of double radio sources, we separate the topic into small-scale (pc) and large-scale (kpc) jets. These two types of objects have have been studied with different telescopes and the two sub-fields have developed largely independently of each other. Very Long Baseline Interferometry (VLBI) with angular resolution of 1 milliarc sec (mas) and better is used at pc scales, and the Very Large Array (VLA) and similar instruments are used for larger scales. VLBI is sensitive only to high surface-brightness features ($\gtrsim 10^5$K) and so typically studies only the core region of a source; whereas the

2

VLA can image the faint outer plumes of a radio galaxy but its core region is subsumed into an unresolved bright spot. This instrumental distinction, however is not definitive, as some observations at certain frequencies cover the intermediate range; *e.g.*, MERLIN and its connections to the European VLBI Network cover a wide range of scales. See Figure 1.1 for a montage of VLBI and VLA images that span the pc-kpc range.

Fanaroff & Riley (1974) showed that the morphologies of extended double radio sources produced by AGN separate into two main classes in a way that correlates with the overall radio source luminosity. In Fanaroff-Riley Class I (FR I) sources, the separation between the regions of highest brightness is *less* than half the largest size of the source, while in Class II (FR II) sources this separation is *more* than half the largest size of the source. For $L_{1.4\text{ GHz}}$ below $\sim 5 \times 10^{25}$ W Hz^{-1} most sources are FR Is, while above this power most are FR IIs. In detail, the break radio power increases with the optical luminosity of the host galaxy (Owen & White, 1991; Ledlow & Owen, 1996); when this dependence is accounted for, the Fanaroff-Riley transition is remarkably sharp (Figure 1.1).
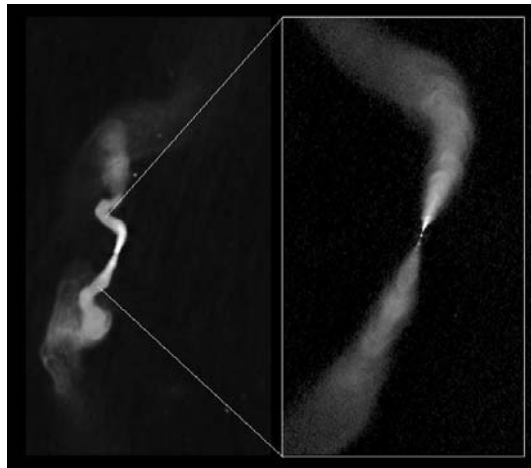

Figure 1.2 VLA images of the plumed Fanaroff-Riley Class I radio galaxy 3C 31: 1.4 GHz, 5.5″ FWHM resolution, 15' (300 kpc) field of view, and (inset) 8.4 GHz, 0.3″ FWHM resolution, 2' (40 kpc) field of view.

3C 31 (Figure 1.2) is an example of a "plumed" FR I source. An unresolved radio *core* at the AGN produces two collimated expanding *jets* that bend and widen into meandering *plumes*. The plumes widen and become fainter away from the core, so that the morphology of the entire source is an edge-darkened structure several hundred kpc in extent whose outer boundaries are ill-defined. At centimeter wavelengths, the spectral indices of such plumes generally increase away from the AGN towards the outer parts of the source, suggesting that the electron populations most affected by synchrotron ageing in such structures are those farthest from the

AGN.

Figure 1.3 VLA image of the lobed Fanaroff-Riley Class I radio galaxy 3C 270: 4.9 GHz, 0.6″ FWHM resolution, 7.5' (70 kpc) field of view.

3C 270 (Figure 1.3) is an example of a "lobed" FR I source. The unresolved *core* produces two expanding *jets*, but the extended structure has a C-shaped outer envelope delineating two *lobes* of more extended emission apparently surrounding the jets. (In 3C 270, the locations of the highest brightness regions are somewhat resolution-dependent, so the classification of the Eastern half of the structure as an FR I is less clear than for the Western half.) The spectral indices of the extended lobes generally increase towards the center of such sources, suggesting that the electron populations most affected by synchrotron ageing are those furthest from the C-shaped envelope. The spectral difference between the extended regions of lobed and plumed FR I sources, and the result that lobed FR I sources are in the majority in complete samples of low-luminosity radio galaxies (Parma *et al.*, 1996) make it unlikely that the lobed sources are bent plumed sources seen in a confusing projection; that possibility cannot be ruled out for individual cases, however.
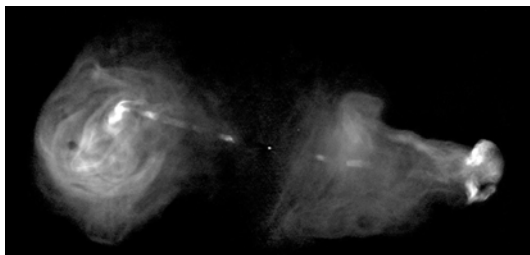

Figure 1.4 VLA image of the Fanaroff-Riley Class II radio galaxy 3C 353: 8.4 GHz, 0.44″ FWHM resolution, 5' (180 kpc) field of view.

3C 353 (Figure 1.4) is an example of a lobed FR II source associated with an elliptical galaxy at $z = 0.03$. The unresolved *core* sits between two well-collimated *jets* that extend towards bright *hot spots* in the outer half of the structure. The more extended emission forms well-bounded *lobes* with much fine structure in filaments,

wisps and secondary hot spots. There is also weak diffuse emission in the center of the source. Compact hot spots are not *required* to be present on both sides of a lobed source for it to be classified as an FR II, but their presence is often a conspicuous difference between lobed FR II sources (like 3C 353) and lobed FR I sources (like 3C 270). There are also significant differences between the jets in the two types of lobed source, see §1.3 where we describe two jet "flavors" whose characteristics correlate well with the Fanaroff-Riley classification of the extended structures that contain them.
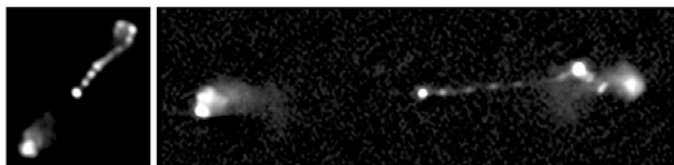

Figure 1.5 VLA images of two Fanaroff-Riley Class II quasars. Left: 3C 212: 8.94 GHz, 0.24″ FWHM resolution, 12″ (∼ 100 kpc) field of view; Right: 3C 204: 4.9 GHz, 0.34″ FWHM resolution, 38″ (∼ 300 kpc) field of view.

3C 204 and 3C 212 (Figure 1.5) are examples of lobed FR II sources associated with quasars at $z \sim 1$. The unresolved radio *cores* and the *jets* are more prominent relative to the extended structure, and the jets are more "one-sided", than in radio galaxies such as 3C 353 (Figure 1.4). Despite the apparent one-sidedness of the jets in these sources, there are often well-defined hot spots in both lobes, suggesting ongoing activity on both sides of the AGN. The lobes of the two quasars shown are also more compact than those in the radio galaxy 3C 353, but this is not always the case — some FR II sources produced by quasars have more diffuse lobes than these, and a few have diffuse extensions resembling the plumes in FR I sources. The spectral indices of FR II source lobes generally increase away from the hot spots at centimeter wavelengths, and are highest in the diffuse emission near the centers of the sources, as in the lobed FR I cases.

1.1.1
Terminology

Several terms used above to describe features of double radio sources have been given precise definitions to assist more fine-grained classification of the radio structures.

Bridle (1986) defined a radio "jet" as "a feature that is at least four times as long as it is wide, separable at high resolution from other extended structures (if any) either by brightness contrast or spatially (*e.g.*, it should be a narrow ridge running through more diffuse emission, or a narrow feature in the inner part of a source entering more extended emission in the outer part), and aligned with the nucleus of the parent object where it is closest to it".

Leahy (1993) defined a "lobe" as "an extended region of emission which is not a jet, showing billowy or filamentary substructure, whose perimeter is mostly well-defined in the sense that the projected magnetic field is parallel to the edge, the intrinsic polarization is $> 40\%$, and the intensity tends to zero as the perimeter is approached."

Bridle *et al.* (1994) defined a lobe "hot spot" as the brightest feature in the lobe having a surface brightness greater than 4 times that of the surrounding emission and a FWHM less than 5% of the largest diameter of the source, while being further from the AGN than the end of the jet if one is detected (to distinguish hot spots from jet knots — see Figure 1.5).

The spectral index, α, is defined by flux density, $S_\nu \propto \nu^{-\alpha}$.

1.2
Parsec scale jets

Most jets are believed to be intrinsically two-sided, because the outer radio structures of the sources are generally symmetric, as in Figs. 1.2 to 1.5 above. However, on a small scale, most jets appear to be one-sided. As explained in Chapter 2, this is due to relativistic boosting, which creates a strong front-to-back ratio when the geometry is propitious; *i.e.*, when $\theta \lesssim \Gamma^{-1}$, where θ is the angle between the jet and the line-of-sight (LOS), and Γ is the Lorentz factor. The boosting greatly raises the apparent luminosity of the approaching jet, so that surveys to a fixed flux density level are strongly biased, and contain one-sided sources well out of proportion to their true numbers in the sky. One-sided jets are discussed here, and compact two-sided jets are considered in 1.2.2.

1.2.1
One-sided jets

Figure 1.6 shows a "stacked" 15-GHz image of the quasar 3C 345, from the MO-JAVE web site [1], showing a one-sided jet. No counterjet is seen. In this case the jet is a stable structure and individual "blobs" or "components" appear near the base and tend to move outward. The stack shows the weighted average of these components, as they move along the track. In other sources the jet is not stable, but can have a variable ejection angle as well as variations in the ridge line.

Figure 1.7 shows the BL Lac object 0003-066 at three epochs. The structure of the jet changes markedly over the ten-year period (Lister *et al.*, 2009a). In another case, 3C 279 (Homan *et al.*, 2003), the jet changed direction over a period of several years, but at a point well downstream of the base. In these cases, it is important to remember that we measure changes in the image as projected on the sky, and small intrinsic bends can be strongly amplified in the projection when θ is small.

In most cases the beginning of the jet is marked by a bright compact component,

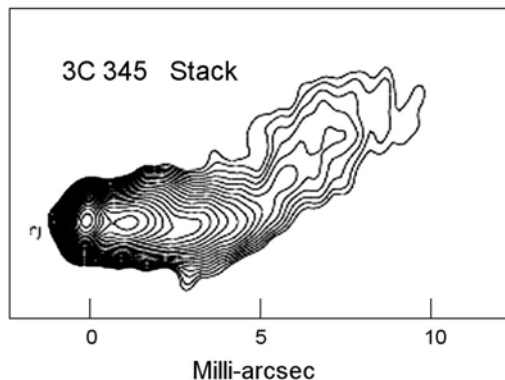1) http://www.physics.purdue.edu/astro/MOJAVE/

Figure 1.6 Stacked image of 3C 345 at 15 GHz. Contours change in steps of $\sqrt{2}$. Thirty-nine separate VLBA images made over the interval 1995-2005 were co-added for this stack (Lister *et al.*, 2009a), which has a dynamic range of about 2000:1. The linear scale is 6.6 pc mas^{-1} so the overall length of the jet seen here is about 60 pc, as projected on the sky.
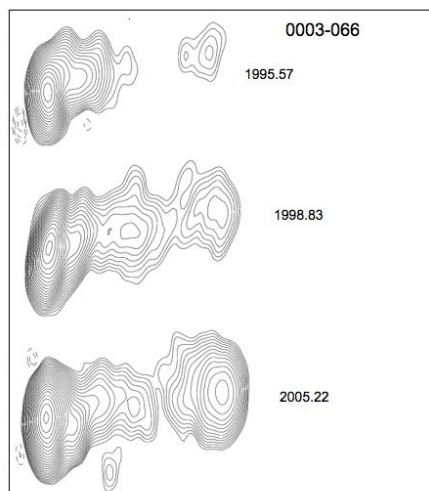
Figure 1.7 Images of quasar 0003-066 at 15 GHz at three epochs: 1995.57, 1998.83, and 2005.22. Images at further epochs can be found at the MOJAVE web site[1], along with a movie. Due to the low declination, the restoring beam is elongated NS. The projected position angle of the jet near the core changes from about $-65°$ to $-110°$ over the 10 years.The projected separation between the two strong peaks in the 2005.22 image is 7.0 mas, or 34 pc.

called the core. It generally is regarded as the location in the jet where the optical depth to synchrotron emission, τ becomes unity, but Marscher (2008) points out that instead it could be a shocked region downstream of $\tau = 1$. The jet generally has decreasing brightness along its length, although strong downstream components often stand out, as in Figure 1.7.

In 1% to 3% of the sources in large VLBI surveys (§1.2.3), the images show only a core. This could be due to insufficient dynamic range, or perhaps to intermittent jet flow.

1.2.1.1 Bends and Helices

Bends such as the one seen in Figure 1.6 are common in pc-scale jets, and they also are seen in large-scale jets; *e.g.*, Figure 1.2. In Figure 1.6 the bend occurs at about $25 \csc \theta$ pc from the center of the host galaxy. As discussed later, θ is probably only a few degrees, so the bend occurs about 500 pc from the center.

The apparent misalignment frequently seen between the ejection at the core and the direction of the large-scale jet was first investigated by Pearson & Readhead (1988) who showed that the distribution of misalignment angles peaked around zero degrees, with a secondary maximum near $90°$. In Figure 1.6, 3C 345 displays a bend of around $40°$, but larger scale images show a total misalignment near $90°$. Conway & Murphy (1993) suggested that this tendency for a $90°$ bend between the small and large scale structure could be due to low-pitch helical motion, combined with relativistic beaming. More recently, however, Kharb *et al.* (2010), with higher-frequency data and more sources, found that the distribution of misalignment angles decreases rather smoothly from $0°$ to $180°$, with only a weak $90°$ peak.

On parsec scales, the shape of a jet projected on the sky is frequently sinuous, and some jets are edge-brightened. This has prompted analyses to describe it as the projection of a helix. Helical structures are expected to occur as a result of nozzle precession, or Kelvin-Helmholtz instabilities (§10.3.1), or via a "magnetic tower" (§4.3.3). Many jets have been analyzed in terms of helices; a few recent ones are for BL Lac (Denn *et al.*, 2000), which yielded $\Gamma = 3 - 6$; 3C 273 (Lobanov & Zensus, 2003) that was fit with a double helix; and 3C 120 (Hardcastle *et al.*, 2005) that was fit in detail, using a "pseudosynchrotron" analysis that included relativistic effects, and showed that a helical expanding jet could match the observations.

1.2.1.2 Wiggles, Wobbles, Kinks

The bends seen in the 3C 273 jet in Figure 1.8 are often called *wiggles*. The jet in 0003-066 (Figure 1.7; z=0.357, scale=4.88 pc per mas) is swinging rapidly, and this is sometimes called *wobble* (Agudo, 2009). The MOJAVE website[1] shows movies of many sources, and the wobble phenomenon can be seen there. The observed time scale for wobble is 2-20 years (Agudo, 2009), although the upper limit probably only reflects the length of time the observations have been made. Wiggles and wobbles are often thought to trace a helical jet; in the latter case the jet is precessing on a short time scale. See Agudo *et al.* (2007) and Britzen *et al.* (2010) for detailed discussions of wobble in the sources 0355+508 and 0735+178,

respectively.

The 3C 273 jet (Figure 1.8) shows a kink in the 15 GHz image, at about 10 mas (projected) from the core. This kink is visible episodically, and sometimes appears to move. See §1.2.4.1 and images on the MOJAVE web site[1]. This structure may represent a kink instability; see Figure 11.9 for a 3D non-relativistic MHD simulation, and §10.3.1.1.
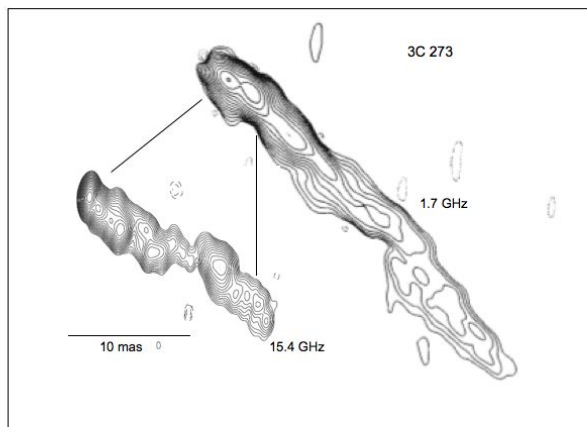
1.2.1.3 Spectrum along a jet, coreshift

Figure 1.8 Images of 3C 273 at 1.7 GHz (epoch 1988.9 (Davis *et al.*, 1991)), and at 15 GHz (epoch 2006.2(Lister *et al.*, 2009a)). The images have dynamic range of about 5000:1. Redshift z=0.158, linear scale is 2.7 pc mas^{-1}. The projected length at 1.7 GHz is about 200 pc, and the true length is a few kpc. Reproduced by permission of NATURE.

The spectrum along a jet generally shows a gradient, with the core having the flattest spectrum (see §7.6.1; this effect is called a 'progression' by X-ray astronomers). This means that observations at lower frequencies usually emphasize the downstream portions of the jet; when combined with the generally lower angular resolution at lower frequencies, this can give a view of the core that is blended with the nearby, steeper-spectrum jet. At higher frequencies the core can be isolated from the downstream jet, and individual components can be seen emerging from the core. For example, in 3C 273 (Figure 1.8) the 1.7 GHz core is composed of a number of 15 GHz components that are blended together. Similarly, the core in the 15 GHz image becomes decomposed at 43 GHz (Jorstad *et al.*, 2005).

The Blandford-Königl model (Blandford & Königl, 1979; Königl, 1981) for the synchrotron emission from an expanding jet shows that there should be a $coreshift$ such that the core ($\tau = 1$ region) moves upstream as the observing frequency is raised. Hence, cores at different frequencies may refer to different locations, and comparison of fluxes or images of such cores should be treated with caution. However, the downstream components are optically thin, and their positions are thought

to be stable as a function of frequency; but see §1.2.4 where the difficulties of following components across frequency are mentioned. Alignment of the optically thin components at different frequencies is a customary way to measure the core-shift (Lobanov, 1989; O'Sullivan & Gabuzda, 2009). Coreshifts are a few tenths of a milli-arcsec at cm wavelengths, in rough agreement with theoretical values.
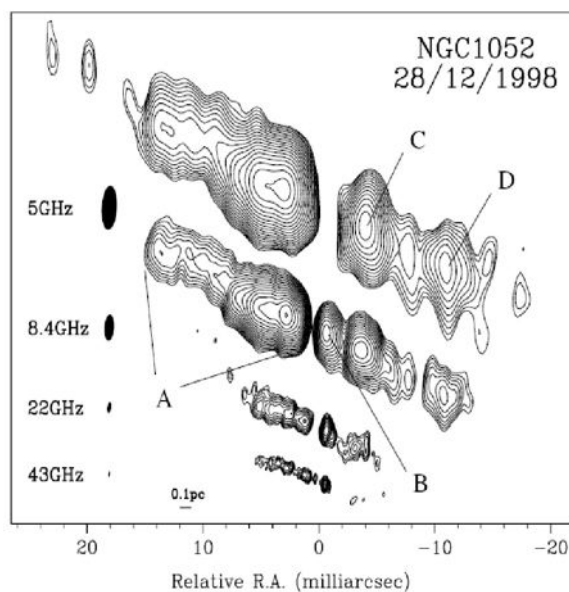
1.2.2
Two-sided jets

Figure 1.9 Images of NGC 1052 at four frequencies. This galaxy is 22 Mpc away so the linear resolution is high, and the overall length of the radio source is only about 4 pc. It is oriented near the plane of the sky, so its projected length is close to the true length. Taken from Kadler *et al.* (2004), reproduced by permission of ASTRONOMY and ASTROPHYSICS.

Lister *et al.* (2009b) discuss five nearby galaxies that have two-sided parsec-scale jets in their nuclei. Their proximity makes them amenable to study with VLBI, even though they have low luminosity and sub-relativistic motions. As an example, NGC 1052 is shown in Figure 1.9 at four frequencies (Kadler *et al.*, 2004). The gap in the center is probably caused by absorption in obscuring clouds, possibly arranged in a torus; the absorption is frequency-dependent and at 5 GHz appears to hide component B. The NE jet is approaching. This source is mildly variable. The components are seen to move outward on both sides, with apparent transverse

speed $v_{app} \sim 0.2c - 0.3c$ (Vermeulen *et al.*, 2003). With the assumption that the two sides are intrinsically similar, $57° < \theta < 72°$ (Kadler *et al.*, 2004), and the true speed of the beam is $v \approx 0.25c$. [Eqs. 2.68, 2.70] The beam in NGC 1052 is not relativistic, in distinction to beams in blazars,

Counterjets are thought to exist in the blazars and radio galaxies, but are rarely seen because they are relativistically deboosted. With sufficient sensitivity, however, the counterjets should be seen. The best cases for this are M 87 (Kovalev *et al.*, 2007), NGC 1275 (3C 84) (Walker *et al.*, 2000), and Cen A (Horiuchi *et al.*, 2006) where weak counterjets are seen with confidence.

Compact Symmetric Objects (CSO) are small but luminous. They have oppositely-directed jets tens or hundreds of parsecs long, and morphologically are often miniature versions of the large extended radio sources. They are young, only thousands of years old, and are expanding but are only mildly relativistic. In some cases there also is large scale outer radio structure, and the CSO may be part of a recurrent phenomenon (O'Dea, 1998). CSOs often have the spectral characteristics of the Compact Steep Spectrum (CSS) and Gigahertz Peaked Spectrum (GPS) sources, which mainly differ by the frequency at the peak of the spectrum: GPS peak above 5 GHZ and CSS peak below that, down to 100 MHz.

1.2.3
VLBI Surveys

Recent major VLBI surveys of compact sources are listed here. The sources are typically selected on the basis of flux density, compactness, and high-energy emission. There is substantial overlap in sources among the surveys. Several of them include subsamples that themselves form a statistically complete, flux-density-limited sample. Most of the surveys are continuing, to increase sample size, to obtain more accurate kinematic data, and to study the relations between the radio and the high-energy emissions, especially gamma-rays measured with the Fermi Observatory.

1.2.3.1 **VIPS, CJF (5 GHz)**
The VLBA Imaging and Polarimetry Survey (VIPS) (Helmboldt *et al.*, 2007) subsumes the 5-GHz Caltech-Jodrell Bank Flat-spectrum survey (CJF; (Taylor *et al.*, 1996)). VIPS includes 1127 sources, most of which are in the SDSS footprint. It comprises a large data base that readily allows radio-optical comparisons, although the SDSS does not have spectral and morphological data for all the objects. The CJF contains 293 objects and is a complete flux-density-limited subset of VIPS. At least three epochs of observations at 5 GHz are available for each CJF source, and images (Britzen *et al.*, 2007), and kinematics (Britzen *et al.*, 2008) are available at their web sites. [2] [3]

2) http://cdsweb.u-strasbg.fr/cgi-bin/qcat?J/A+A/472/763
3) http://cdsweb.u-strasbg.fr/cgi-bin/qcat?J/A+A/484/119

1.2.3.2 **MOJAVE (15 GHz)**

MOJAVE (Monitoring Of Jets in Active galactic nuclei with VLBA Experiments) (Lister *et al.*, 2009a) is a 15-GHz monitoring survey that currently is being expanded to include about 280 sources. It includes a statistically complete subsample of 163 objects, the known compact sources stronger than 1.5 Jy at any epoch since 1994, and north of $\delta = -30°$. Full polarization images of each source are made at each epoch. The cadence for observing the sources varies from three weeks for rapidly moving complex sources, to about two years for more stable objects. The median number of epochs per source is about 10; this is sufficient for accurate measurements of component motions.

MOJAVE is a continuation of the 2-cm VLBA survey that started when the VLBA became available in 1994 (Kellermann *et al.*, 1998). The main objectives of the program include studying the internal motions and polarizations of the sources, and correlating the high-resolution radio results with gamma-ray emissions as measured by the Fermi satellite. Data and results from MOJAVE are available at their website[1].

1.2.3.3 **TANAMI (8.4, 22 GHz)**

The MOJAVE survey has a restricted declination range, and to cover the whole sky the southern-hemisphere TANAMI program (Tracking Active galactic Nuclei with Austral Milliarcsecond Interferometry) was instituted. It is monitoring strong compact sources south of $\delta = -30°$ with VLBI at 8.4 and 22 GHz. It includes flat-spectrum radio sources with flux density above 2 Jy at 5 GHz plus a number of other sources of interest, including gamma-ray sources seen by the LAT on the Fermi Observatory, This program is still at an early stage, but has published first-epoch results at 8.4 GHz on 43 objects. (Ojha *et al.*, 2010)

1.2.3.4 **VCS1 (2, 8 GHz)**

The VLBA Calibrator Survey (VCS1) (Beasley *et al.*, 2002) includes 1332 compact sources observed with the VLBA at 2.3 and 8.4 GHz with astrometric accuracy. The objective is to provide a list for phase referenced VLBI observations, and for astrometry and geodesy. The data are also useful for astronomical studies of compact jets.

1.2.3.5 **RRFID (2, 8 GHz)**

The RRFID (the US Naval Observatory's Radio Reference Frame Image Database) supports precision astrometry and geodesy by maintaining a large data base [4]. of images of compact radio sources (Fey *et al.*, 1997a; Fey & Charlot, 1997b, 2000). Observations are performed every other month at 2 and 8 GHZ, using the VLBA together with up to 10 geodetic antennas. Currently the database contains 517 sources, chosen for their suitability for astrometry and geodesy. The *RRFID kinematic survey* (Piner *et al.*, 2007) is a subset of the data base comprising 87 sources with at least three epochs of observation at 8 GHz.

---

4) http://orf.usno.navy.mil/RRFID

1.2.3.6 **VSOP (5, 22 GHz)**

The VSOP (VLBI Space Observatory Program) included a pre-launch survey (Moellenbrock *et al.*, 1996) that detected strong fringes from 136 sources at 22 GHz, and provided a guide for the main program between the HALCA (Highly Advanced Laboratory for Communications and Astronomy) satellite and the ground-based VLBI antennas. In the satellite program 242 sources were studied (Dodson *et al.*, 2008).

Measurment of brightness temperatures of AGN cores was a major part of the program. HALCA baselines were 3 times longer than those available between two telescopes on earth, and so in principle should have yielded brightness temperatures (or limits) an order of magnitude larger than those available from terrestrial measurements. However, noise and calibration difficulties on the long baselines to the satellite reduced the available T_b range in some cases. See §1.2.6.

1.2.3.7 **43 GHZ survey**

Jorstad *et al.* (2005) made VLBA observations of 15 AGN at roughly 2-month intervals during 1998-2001, at 43 GHz. Both total and polarized images of the flux density were obtained. This is the largest published set of multi-epoch VLBI observations that exists at millimeter wavelengths. The targets include objects that are bright and variable at 43 GHz, and the objective is to gain information relevant to jet collimation and acceleration, and to evaluate correlations between gamma-ray emission and the radio structures. This work has continued, currently with monthly observation of about 30 blazars with the VLBA. Images and model details are available on their website[5].

1.2.3.8 **GMVA (86 GHz)**

VLBI at 86 GHz is important but difficult. At this frequency the core of a jet may be optically thin, and so allow a view deep into the central region of the AGN. The resolution is high since a global array has $d/\lambda > 2 \times 10^9$; this corresponds to less than 60 Schwartschild radii at a nearby object like M 87 (Krichbaum *et al.*, 2007).

Lee *et al.* (2008) have made a survey of 127 sources with the GMVA (Global Millimeter VLBI Array) at 86 GHz, of which 109 yielded images. The dynamic range is low but some of the soures show several components and can be said to have a jet-like structure.

1.2.4
Motions in the jet

The components seen along the jets in Figures 1.6-1.9 tend to move downstream, away from the core. Multi-epoch images are used to track their motions, as in Figure 1.10, where the distance of the centroid of each component from the core is plotted. Figure 1.10 shows a simple case, where there is no ambiguity in following the components. Often, however, components are close together and some follow
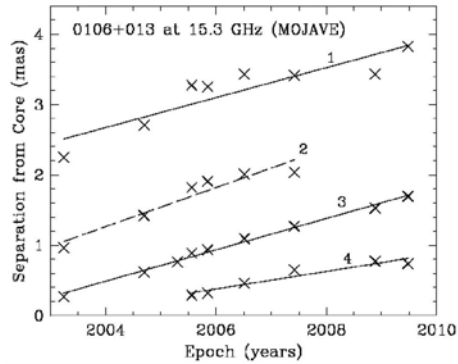
---

5) http://www.bu.edu/blazars/research.html

Figure 1.10 Expansion diagram for four components in 0106+013. Solid lines indicate uniform vector motion that is radial, to within the uncertainties, while the dashed line for component 2 indicates a significantly non-radial motion Lister *et al.* (2009b).

curved trajectories, and in complex cases it is necessary to make observations at close intervals to follow the components unambiguously. Many examples are in the literature, see *e.g.*, Lister *et al.* (2009b) at 15 GHz and Jorstad *et al.* (2005) at 43 GHz. The slope of the trajectory gives a speed that is usually expressed as a multiple of the velocity of light; see §1.2.5.

The RRFID survey at 8.6 GHz is closely matched in resolution to the MOJAVE survey at 15 GHz, because RRFID has longer baselines that roughly compensate for the longer wavelength. Piner *et al.* (2007) have used this fact to compare the motions at the two frequencies for the 36 sources they have in common. For a few components in certain sources the motions are in good agreement; but for most components they are not. (See Figure 8 of Piner *et al.* (2007)) If angular resolution is not the cause of these disagreements, what is? It likely results from time-dependent spectral differences among the various components, combined with difficulties in identifying components in the images, and differences in modelling techniques. More work is needed to clarify the frequency dependence of component identifications.

A substantial fraction of the moving components are not moving radially out from the core (32% at 15 GHz in the MOJAVE survey). In these cases a plot like Figure 1.10 can be misleading. Several of the surveys described above present data on both radial and transverse components of the velocity. In addition, some components are seen to accelerate, either by changing direction or by changing speed with a constant direction.

In all surveys, a small number of sources are found that have components moving towards the core. These appear in sources that otherwise are normal, and explanations for this behavior have been offered within the relativistic outflow model. See *e.g.*, Britzen *et al.* (2007), Lister *et al.* (2009b). The first is that as a component moves downstream around a bend, its projected position can move towards the

core, and it could even move behind the core and emulate a counterjet. Secondly, as a new component begins to emerge from the core, the centroid of the enlarged core moves downstream, meaning that the separation of this centroid from the next component can get smaller. Orienti & Dallacasa (2010)

1.2.4.1 **Ballistic vs streaming motions**

An early question was whether the bends are formed by dynamical processes, with the components streaming along the jet; or the flow is ballistic, with bends formed by rotations of the nozzle. It now is clear that this question is too simplistic, since both types of motion can occur in the same source. 3C 345, however, presents a clean case of streaming around a bend. (Figure 1.6) The bend at 4 mas was stable for 14 years, while the speed of the individual blobs was about 0.56 mas/yr (Lister *et al.*, 2009b). Had the flow been ballistic, the bend would have been substantially broadened to the west. As it is, individual components were tracked going around the bend. (See Lister *et al.* (2009b), Figure 3.340)

The motions in 3C 273 are more complex. The position angle (PA) at the nozzle was about $144°$ in 2006, as seen at 15.4 GHz in Figure 1.8. However, this angle is resolution-dependent; if 3C 273 had been farther away, or if the observations had been made at a longer wavelength, the PA would have appeared to be smaller. The kink near 10 mas connects regions that are offset but roughly parallel; this feature appears in 3C 273 at many epochs. During some intervals the kink appears to move out with the flow; see the sequence of images and the movie in the MOJAVE web site [1], especially the interval 2004-2008. Another feature of 3C 273 is that the initial PA itself changes, *e.g.*, from about $110°$ in 1995 to about $144°$ in 2006, at 15 GHz. Abraham & Romero (1999) modelled 3C 273 with a precessing helix, with a period of about 16 years; while Lobanov & Zensus (2003) used a double helix to allow for the tranverse structure in the jet.

1.2.4.2 **Pattern vs Beam**

Another early question was whether VLBI was measuring relativistically moving blobs of plasma, or patterns such as those formed on a screen, or by stationary but blinking lights. Several lines of evidence show that the radiating plasma is indeed moving. First, there is strong evidence for relativistic motion, as described in Chapters 1 and 2 and in §5.3.1. Secondly, the fact that 95% or more of the moving components are moving out, not in, eliminates random motions. Thirdly, statistical studies of strong radio jets show that the apparent luminosity is correlated with the apparent transverse speed, as expected for relativistic beams (§1.2.6). This would require an *ad hoc* explanation for screens.

However, there may well be a difference between the motion of the underlying flow and that of a visible moving radio component. The enhanced density responsible for the component may be due to a shock, whose apparent speed and direction will be different from that of the general flow. (Chapter 9) A stationary shock could produce a stationary component, and indeed many of these are seen. Low-pattern-speed (LPS) features in the MOJAVE sample have been studied by

Lister *et al.* (2009b), who show that most LPS components are found within 6 pc (projected) of the core. They may be due to standing shocks, possibly generated at a bend in the jet. Some of them could simply reflect the geometry; for example, a helical beam could have its Doppler shift enhanced at a stationary point where the beam lies close to the LOS. See (Roca-Sogorb *et al.*, 2010) for a discussion of a new stationary component that suddenly appeared in 3C 120.

Some components may be due to trailing shocks (*e.g.*, Agudo *et al.* (2001)) that are slower than the flow; use of such components will underestimate the flow velocity. The use of the fastest component to derive the Lorentz factor (Lister *et al.*, 2009b) will yield a velocity that will overestimate the flow speed if that component is a density enhancement in a downstream shock.

1.2.5
Relativistic beams

Relativistic beams are discussed in Chapter 2, and the results developed there are used here. A moving component is characterized by its Lorentz factor, Γ, and the angle to the LOS, θ; from these the Doppler factor, δ, and the normalized apparent transverse speed, $\beta_{\mathrm{app}} = v_{\mathrm{app}}/c$ can be found (Eqs. 2.30, 2.59). When $\Gamma^2 \gg 1$, the beam parameters are simply related as in Figure 2.6, which shows β_{app} and δ vs θ, all normalized by Γ. Note that the peak Doppler factor is approximately twice the Lorentz factor and is attained when $\theta = 0°$. When $\sin\theta = \Gamma^{-1}$, $\delta = \Gamma$ and $\beta_{\mathrm{app}} = \beta_{\mathrm{app,max}} = \beta\Gamma$. This value of θ is called the "critical angle," θ_{crit}, or the "superluminal angle," θ_{sl}. (§2.3.2)

When $\Gamma > \sqrt{2}$, then $\beta_{\mathrm{app}} > 1$ in some range of θ, in which case the apparent motion is said to be superluminal. Another relativistic effect is a reduction in apparent time intervals, proportional to δ. This increases the apparent flux density variability. The MOJAVE survey includes sources whose flux density has exceeded the lower limit at some time during the specified program interval. Thus the list is biased towards sources with rapid variability; i.e. high Doppler factor, which implies high Lorentz factor, because $\Gamma > \delta/2$.

The flux density received from an approaching relativistic beam is increased by a factor of δ^n over what a co-moving observer would measure, where $n = p + \alpha$; α is the spectral index and p is the Doppler boost index, typically 2 or 3. See Figure 2.3 and Eq. 2.44. The exponent $p = 3$ is appropriate for the radiation from a sphere, but $p = 2$ for a continuous jet (Lind & Blandford, 1985); see also §1.2.7. Since δ can be 20 and more, it is clear that beams aimed close to the LOS can be greatly magnified in strength, and those aimed in other directions will be weakened. This biases the selection of beamed sources; a sample chosen on the basis of the beamed flux density will preferentially contain sources with small values of θ, even though the solid angle associated with powerful boosting is small (Scheuer & Readhead, 1979). With a simple model for a flux density-limited sample of beamed sources, Cohen *et al.* (2007) showed that roughly $3/4$ of the sample will have $\theta < \theta_{\mathrm{crit}}$. A further implication is that the parent population of the observed relativistic sources must be huge; Lister & Marscher (1997) estimate

that there are millions of mis-directed AGN to provide for the 293 objects in the CJF survey.

1.2.5.1 **Superluminal Motion**

A source will typically produce a new moving component every few years, and in some sources many components have been followed. In Figure 1.10 four components are labelled, and it is noticeable that their lines are roughly parallel; they have similar speeds. In MOJAVE (Kellermann *et al.*, 2004) and RRFID (Piner *et al.*, 2007) the variance of the speeds in a source is less than the variance of the speeds among all sources, so many sources can be said to have a characteristic speed. In fact most sources are not as clean as 0106+013 (Figure 1.10), and many have both stationary and moving features.
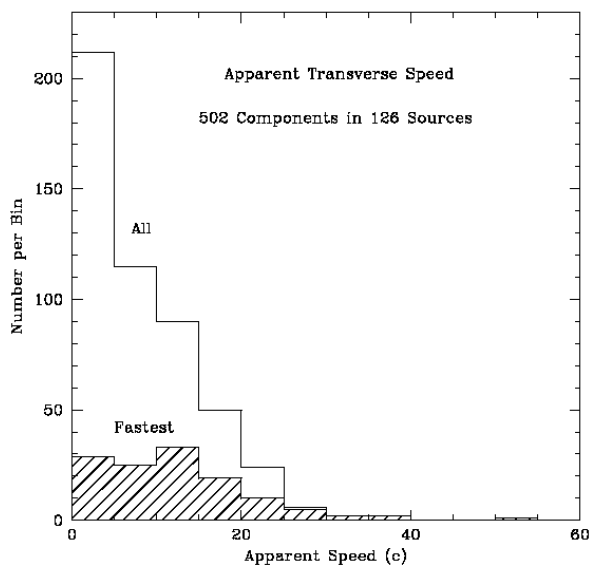

Figure 1.11 Histograms of β_{app} for MOJAVE; open for all robust components, and hatched for the fastest component in each soure. From Lister *et al.* (2009b), Figure 7.

Although there is difficulty in following individual components at different frequencies, the statistics of the speeds can give useful information. Lister *et al.* (2009b) use the *fastest* moving component for studying the MOJAVE sources, because that might best represent the speed of the underlying flow; slower components might be due to trailing shocks, which are slower than the flow (Agudo *et al.*, 2001). Figure 1.11 shows the distribution of β_{app} for the MOJAVE sample. The open line is for all robust jet features, and the solid histogram shows the fastest robust component for each source. The distribution of the fastest components is

roughly flat to $\beta_{\mathrm{app}} \sim 15$ with a tail to $\beta_{\mathrm{app}} = 50$. The distribution of all features has a strong peak at low speeds; 40% of all features have $\beta_{\mathrm{app}} < 5$.

CJF is also a flux-limited survey, but a comparison with MOJAVE is difficult because the results are reported differently. Figure 7 in Britzen *et al.* (2008) shows a histogram of speeds for all "quality 1" components, but this includes more than one point for some sources. The shape of the histogram is similar to the open line in Figure 1.11, but is narrower, with a tail to $\beta_{\mathrm{app}} \sim 25$. The 5 GHz speeds on average are lower than the 15 GHz speeds, very roughly by a factor of 2. See Britzen *et al.* (2008) for further discussion.

RRFID and the 43 GHz survey do not use complete samples, but rather concentrate on particularly bright and compact sources. However, CJF and MOJAVE are restricted to *flat-spectrum* sources, which in general are bright and compact, and there are many sources in common among these four surveys. At 8 GHz, RRFID shows a histogram of 54 speeds, for the fastest component in each source. It is similar to the 15 GHz plot, roughly flat to $\beta_{\mathrm{app}} \sim 10$ with a tail to $\beta_{\mathrm{app}} \sim 30$, but with a peak in the first bin (0-2c). Jorstad *et al.* (2005) study only 15 sources and an equivalent histogram is not warranted. However, from their Table 5 we find that at 43 GHz the median of the fastest average speeds is $\beta_{\mathrm{app,med}} \approx 17$. From these comparisons, it appears that the fastest speeds increase as the observing frequency increases from 5 to 43 GHz. Lister *et al.* (2009b) suggest that at the higher frequencies superior resolution and reduced sampling interval allow the faster components to be detected more easily. Furthermore, as seen in Figure 1.8, a component can be a blend of higher-frequency components, and if there is a distribution of speeds among the components it is only at the higher frequency that the fastest speed can be detected.

1.2.5.2 **Lobe-Dominated Quasars**

Most of the radio studies involving relativistic beams use objects whose jets lie close to the LOS; the cores and jets are strong and amenable to study. The more numerous jets lying close to the plane of the sky are strongly de-boosted and invisible. But an intermediate angular range, roughly from $10°$ to $40°$, is being studied, albeit with difficulty. Hough *et al.* ((Hough *et al.* , 2002; Hough , 2008)) are observing a complete sample of 25 weak-nucleus *lobe − dominated quasars* (LDQ) from the 3CR catalog, with the VLBA. They have made images of all the objects, and have found that 22 have one-sided jets; the other three are barely resolved. For ten of the objects speeds have been determined, and they fall in the range $\beta_{\mathrm{app}} \sim 0$ to 10. The LDQ appear to be physically the same as the strong core-dominated quasars, but at higher angles to the LOS.

1.2.6
Statistical studies of compact jets with VLBI

The Lorentz factor Γ is an important physical quantity that characterizes a beam, but it can be estimated only indirectly. The measured distribution of β_{app} (Figure 1.11)

shows that there must be a distribution of Γ, for if all sources had the same Γ, then the distribution of β_{app} would have a sharp peak at $\beta_{app} \approx \Gamma$, which it does not have (Lister & Marscher, 1997; Vermeulen & Cohen, 1994). A power-law distribution has generally been used in statistical studies involving Γ (Lister & Marscher, 1997).

The observable quantities are flux density, brightness distribution, redshift and proper motion, and from the latter two the apparent transverse speed β_{app} is calculated. In a number of cases where both a jet and counter-jet are seen (or where useful limits can be set) the Doppler factor has been estimated by assuming that the two jets are intrinsically identical, as discussed in Chapter 2. Once β_{app} and δ are in hand, then Γ and θ can be calculated with Eqs. 2.71 and 2.72.

For a one-sided source, it is sometimes assumed that $\Gamma \approx \beta_{app}$ (*i.e.*, that $\theta \approx \theta_{crit}$). However, this will be incorrect in many cases. From Monte-Carlo simulations with a power-law distribution of Lorentz factors, Cohen *et al.* (2007) showed that $\Gamma > 1.5\beta_{app}$ for roughly 30% of the the sources with $\beta_{app} > 4$, in a flux density-limited sample of relativistic jets.

The Doppler factor δ may be estimated from the brightness temperature of the jet, T_b, which can be directly measured with VLBI. The Doppler factor is found by dividing T_b by an "intrinsic temperature," T_{int} (Eq. 2.49), usually taken to be the "equipartition temperature," $T_{eq} \sim 5 \times 10^{10}$K defined by Readhead (1994); or a limit can be found by using the Inverse-Compton limit $T_{IC} \sim 10^{12}$K (Kellermann & Pauliny-Toth, 1969). δ and β_{app} then uniquely fix the value of Γ (Eq. 2.71). Homan *et al.* (2006) separate the MOJAVE observations into low and high flux-density states, and show that in the low state $T_{int} \sim 3 \times 10^{10}$K, and in the high state $T_{int} \geq 2 \times 10^{11}$K. For sources in the high state the median of the peak values of T_b is $\sim 2 \times 10^{12}$K, and the lower limits on T_b extend up to 5×10^{13}K (Kovalev *et al.*, 2005). If we take $T_{int} \sim 2 \times 10^{11}$ then $\delta_{med} \sim 10$ and δ_{peak} is at least 250, although it may be the case that T_{int} is higher for sources with higher brightness temperatures, and δ_{peak} correspondingly lower. In most cases $\delta > \Gamma > \delta/2$ (Cohen *et al.*, 2007), so Γ_{med} is between 5 and 10.

The VSOP has T_b results (Dodson *et al.*, 2008) that are similar to those for MOJAVE. The measured values have a median of about $10^{12.1}$K, while including the limits would probably increase the median. There is little difference in T_b between 5 and 15 GHZ, as expected for optically thick synchrotron cores having the same Doppler factors at the two frequencies.

A brightness temperature $T_{b,var}$ can also be estimated from the time-scale for flux-density variability. The cube root of the ratio of $T_{b,var}$ to T_{int} gives the "Variability Doppler factor" D_{var} that, with β_{app}, gives the Lorentz factor. See Eq. 2.50; also Lähteenmäki & Valtaoja (1999). Jorstad *et al.* (2005) developed a method that also uses the flux density variability but with the measured angular diameter, not an assumed intrinsic temperature. The various estimates for Γ agree reasonably well for the Jorstad sample, and lead to distributions of Γ that peak at $\Gamma \sim 20$ with a tail to $\Gamma \sim 40$ for quasars, and lower values for BL Lac objects and radio galaxies. However, since $\Gamma > \beta_{app}$ and the fastest speeds at both 15 and 43 GHz are near $\beta_{app} = 50$, it is clear that the distribution of Γ must extend up to at

least $\Gamma = 50$.
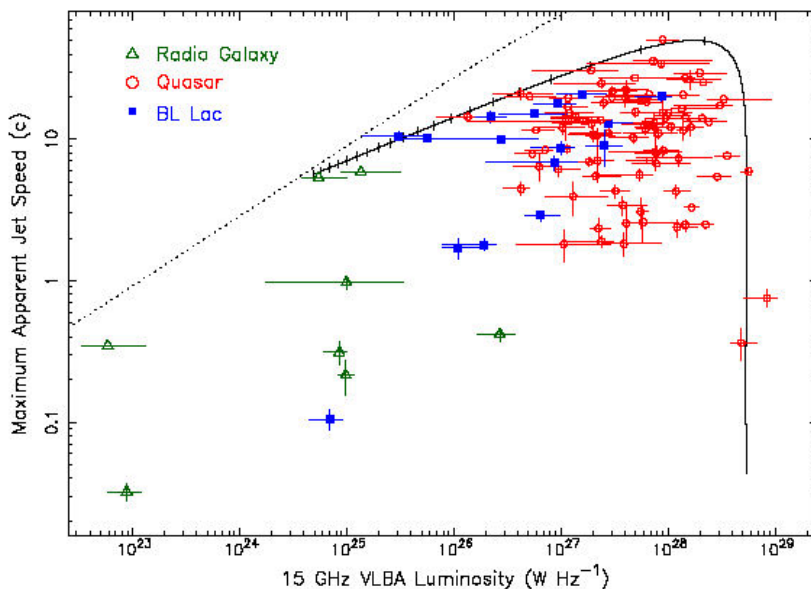
1.2.6.1 **Luminosity-speed correlation**

Figure 1.12 Maximum apparent jet speed vs. VLBA luminosity at 15 GHz for 121 jets in the MOJAVE sample. Circles indicate quasars, squares BL Lac objects, and triangles, galaxies. Horizontal bars indicate the range of luminosity during 1994.0-2004.0. The curve is parametric in θ, see text. Adapted from Lister *et al.* (2009b).

Figure 1.12 shows the peak apparent speed and median apparent luminosity for 121 jets in the MOJAVE sample. The line is an "aspect curve" Cohen *et al.* (2007), the run of $(\beta_{\mathrm{app}}, \mathrm{L}_{\mathrm{app}})$ for a jet with $\Gamma = 50$ and an intrinsic luminosity $\mathrm{L_o} = 3 \times 10^{25}$ W Hz^{-1}, Doppler-boosted by a factor $\delta^{1.63}$, as θ increases from $10''$ at the right-hand end through $1.1°$ at the peak to $23°$ at the left end. Cohen *et al.* (2007) and Lister *et al.* (2009b) show that the lack of sources to the left of the line is not a selection effect, but represents a real correlation between speed and luminosity: low-luminosity sources do not have high-speed components. This is seen also in the 5 GHz CJF sample (Britzen *et al.*, 2008).

It is tempting to regard Figure 1.12 as showing that the strongest sources in the sky have $\Gamma \approx 50$ and $\mathrm{L_o} \approx 3 \times 10^{25}$ W Hz^{-1} at 15 GHz. There are only a few of these objects and they are at various θ; the ones with $\theta \lesssim 2°$ lie near the line in Figure 1.12, at the right-hand side and at the top. The ones with higher θ, however, are increasingly unlikely to be in the survey. Cohen *et al.* (2007), using probability arguments, showed that sources near the line but with $\theta \gtrsim 2°$ have lower values of Γ and $\mathrm{L_o}$. These studies assumed that the distributions of both the intrinsic

luminosity and Γ for a population of beamed jets have power-law shapes. The luminosity functions have been studied by Lister & Marscher (1997) and Cara & Lister (2008).

1.2.7
Spine-sheath configuration

The nearby galaxy M 87 has a long jet that can be studied in detail, and it displays notable transverse structure. It is $edge-brightened$; see *e.g.*, Kovalev *et al.* (2007); Ly *et al.* (2007) for images at 15 and 43 GHz, respectively. This is thought to be due to a transverse velocity gradient, with the jet velocity faster on-axis than at the edge, where there is a slowly moving "sheath". The viewing angle is greater than the critical angle for the the central spine, $\theta > \theta_{\mathrm{crit,spine}}$ so that the spine is deboosted, but $\theta < \theta_{\mathrm{crit,sheath}}$ and the radiation from the limb is relativistically enhanced. Spine-sheath models in an X-ray context are discussed in Chapter 7, and numerical simulations are in Chapters 10 and 11. See (Laing & Bridle, 2002a) for an analysis of 3C 31 that leads to a transverse velocity gradient in a large-scale jet.

The radio galaxy Cygnus A may be similar to M 87. Cohen *et al.* (2007) suggest that its powerful radio lobes are indicative of a highly relativistic spine that is invisible because of its large angle, while it has a mildly relativistic sheath that produces the observed weak jet and counter-jet.

The spine-sheath jet configuration is also useful in population studies. The unification of FR I radio galaxies with BL Lac objects, with the galaxies being off-axis BL Lacs, has difficulty that is eased if the Doppler factor that controls the galaxy luminosity is smaller than the one that controls the superluminal motion (Chiaberge *et al.*, 2000). An object that has a spine-sheath configuration will have an angular dependence of flux density that varies with θ more slowly than the canonical δ^p, with $p = 2$ or 3.

1.3
Kiloparsec-scale jets

1.3.1
Correlations with extended structure and luminosity

Many properties of kpc-scale radio jets produced by AGN correlate well with other features of the radio sources, as follows.

- **Correlations between jet properties and the Fanaroff-Riley structure classes:**
  The kpc-scale jets in low-luminosity FR I radio galaxies are generally prominent (often $> 10\%$ of the total extended radio power), rapidly spreading (FWHM opening angles $> 8°$), and "two-sided" (jet-counterjet intensity ratio $< 4 : 1$), whether the large scale structure is plumed (*e.g.*, Figure 1.2) or lobed (*e.g.*, Figure 1.3). Those in higher-luminosity FR II sources are better collimated, more

"one-sided", and are generally less prominent relative to the lobes (Bridle, 1984) in radio galaxies (*e.g.*, Figure 1.4) than in quasars (*e.g.*, Figure 1.5).

- **Correlations between kiloparsec and parsec scales:** The brighter kpc-scale jet is always a plausible extension of the brighter parsec-scale jet and is always on the same side of the source as any superluminal motion (see Sec 1.2.5.1). The kpc-scale jets are also well aligned with the parsec-scale jets in the FR I sources (Giovannini *et al.*, 1994; Venturi *et al.*, 1994, 1995) and in lobe-dominated FR II sources. In core-dominated sources (whose jets may lie closer to the line of sight where *angular* relationships can be exaggerated by projection) even when the jets appear more bent the brighter large-scale jet is generally a plausible continuation of the brighter small-scale jet. These correlations imply that the initial brightness asymmetries of the jets on both parsec and kiloparsec scales, and the superluminal motions, all share a common explanation as consequences of bulk relativistic outflow from the AGN.

- **Correlations between jet sidedness and depolarization asymmetry:** In sources whose kpc-scale jets differ greatly in brightness, the brighter jet is on the side of the source that depolarizes less at long wavelengths (Laing, 1988; Garrington *et al.*, 1988, 1991; Parma *et al.*, 1996; Morganti *et al.*, 1997). This is consistent with the brighter jet being on the side of the source that has the shorter path length to the observer through any intervening Faraday-rotating medium, hence with the apparently brighter jet always being on the side that is nearer the observer, as required if the brightness asymmetry is (primarily) due to relativistic aberration.

- **Correlations between magnetic field orientation and jet sidedness:** Well-resolved kpc-scale jets are often highly linearly polarized, so their magnetic fields must be partially ordered transverse to the line of sight. Sensitive, resolved polarimetry shows that the "one-sided" jet features (*i.e.*, all of the jet lengths in FR II sources and the brighter regions near the bases of "two sided" jets in FR I sources) are dominated by field components oriented *parallel* to the jet axes. Straight segments of kpc-scale jets in FR I sources usually become dominated by apparently *perpendicular* field on the jet axes far from the AGN (Bridle, 1984), while parallel field may still prevail at the jet edges (see §1.4.2 below) and on the outsides of pronounced bends in the jets.

1.3.2
The two jet 'flavors'

Kiloparsec-scale radio jets evidently come in two principal flavors (Bridle, 1991; Laing, 1993) whose properties are closely related to the Fanaroff-Riley structure classes:

- *Weak-flavor jets:* prominent, mostly "two-sided", rapidly spreading, dominated by perpendicular magnetic field near the axis over much of their length, and terminating either in meandering plumes or in lobes without hot spots to form low-luminosity FR I sources.

- *Strong-flavor jets:* less prominent in radio galaxies than in quasars, mostly "one-sided", narrowly spreading, dominated by parallel magnetic field over much of their length, terminating at hot spots to form luminous two-lobed FR II sources.

The side-to-side brightness asymmetries of the inner, straighter segments of weak-flavor jets decrease both with distance from the AGN and towards the outer edges of these jets (Laing, 1996; Laing *et al.*, 1999). However, in both plumed and lobed FR I sources, the asymmetries of the most extended structures usually become *more* marked further from the AGN. The first trend suggests that the *initial* asymmetries of weak-flavor jets arise from relativistic aberration, but also that relativistic asymmetries decrease with distance from the AGN due to jet deceleration. In contrast, environmentally-induced asymmetries grow with distance from the AGN and eventually dominate those due to aberration. The clear continuity of jet brightness asymmetries between the parsec and kiloparsec scales in individual sources supports the notion that the radio asymmetries are dominated on small scales by relativistic effects, but on large scales by environmental effects. In strong-flavor jets, however, it appears that significant effects of relativistic aberration persist at least as far as the terminal "hot spots", and perhaps somewhat beyond them.

1.3.3
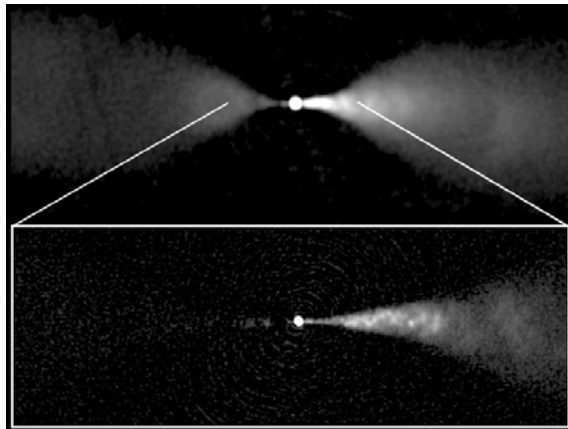### Internal structures of kpc-scale radio jets

Figure 1.13 Structures at the kpc-scale base of the jet and counterjet in the FR I radio galaxy NGC 315. Upper: VLA 4.9 GHz with 2.35″ FWHM resolution, 300 ″ (100 kpc) field of view. Lower: VLA 4.9 GHz with 0.36″ FWHM, 60″ (18 kpc) field of view.

Figure 1.13 illustrates typical structures found near the bases of weak-flavor jets using the well-resolved example of NGC 315 (Laing *et al.*, 2006b; Worrall *et al.*, 2007).

1.3.3.1 **Spreading rates**

Neither weak nor strong flavor jets appear to be freely-expanding (*i.e.*, conical) outflows on kpc scales. Rather, there is evidence that both flavors continually interact with, and adjust to, their environs.

Weak-flavor jets that have been resolved transverse to their axes always begin well-collimated and faint, then *brighten* and *flare*, *i.e.*, spread much more rapidly, a few kpc from the nucleus. At high resolution, the brightening region often contains off-axis discrete knots, as well as a more general increase in intensity. *Brightening* usually precedes geometric *flaring* (as in the upper panel of Figure 1.13) but the two effects can occur close together *e.g.*, in 3C 31 (Laing & Bridle, 2002a). Most weak-flavor jets recollimate, *i.e.*, revert to less rapid spreading, further from the AGN. Some exhibit several distinct episodes of fast spreading followed by recollimation (*e.g.*, near the center of Figure 1.3 where the lobes are faint relative to the jets).

Strong-flavor jets spread more slowly than weak-flavor jets (Bridle, 1984) and variations in their spreading rates are less evident far from the AGN. Note however that as FR II sources are generally more luminous than FR I sources, there are fewer nearby examples so their jets are harder to resolve; 3C 353 (Figure 1.4, Swain *et al.* (1998)) is the best-resolved.

In some lobed FR I sources where jets appear to be surrounded by more extended radio emission (at least in projection) the counterjets appear to spread more rapidly than the brighter main jets. §1.5 suggests a possible explanation for this.

1.3.3.2 **Transverse brightness profiles**

The counterjets in weak-flavor jets are less strongly center-brightened than the main jets close to the AGN; some are noticeably center-darkened. The transverse profiles of total intensity are generally symmetric away from sharp bends or localized knots.

The few strong-flavor jets that have been well resolved in the transverse direction show limb-brightening or flat-topped emission profiles away from bright knots (Carilli *et al.*, 1996; Swain *et al.*, 1998). The apparent suppression of emission near the jet axis implied by these profiles could have two causes: (a) differential Doppler boosting between a fast relativistic spine and a slower-moving boundary layer and/or (b) intrinsically enhanced emissivity in the boundary layer (*e.g.*, from *in situ* particle acceleration or magnetic field amplification by velocity shear). Whichever effect predominates, visualization of emission features in strong-flavor jets appears to be biased toward their (possibly slowest-moving) outer layers. Higher angular resolution and sensitivity (*e.g.*, the EVLA) are needed to explore this effect more thoroughly, and detections of strong-flavor counterjets might distinguish the two ways of explaining the transverse intensity profiles. Strong edge brightening has also been seen in the well-resolved, and notably "one-sided" pc-scale jet in M 87 (Kovalev *et al.*, 2007), in which measured proper motions are small.

1.3.3.3 **Polarization and magnetic field orientation**

There is a characteristic asymmetry across the AGN in the degree and direction (corrected for Faraday rotation) of linear polarization of weak-flavor jets which

correlates well with the asymmetry in total intensity: the base of the brighter jet has a polarization minimum on-axis which always extends further from the nucleus than its equivalent in the counterjet. Before the polarization minimum, the apparent magnetic field on the axis is oriented *along* the jet. After the minimum, the apparent magnetic field is oriented *across* the jet. In both the main jet and the counterjet, the *transverse* profiles of the degree of polarization and total intensity are usually quite symmetric in regions away from bright local knots.

This strong coupling of the asymmetries in the linear polarization and intensity of weak-flavor jets is a key to modeling them as intrinsically symmetrical *decelerating* relativistic outflows (§1.4).

The faint inner regions of weak-flavor kpc-scale jets resemble strong-flavor jets in that they are well-collimated and dominated by magnetic field components parallel to the jet axis. *All well-studied weak-flavor jets undergo a transition in which their collimation and magnetic structure change dramatically near the distance from the AGN where their sidedness also changes rapidly.* Elucidating the physics of this transition region in the weak-flavor jets is clearly important for understanding the relationship between the two jet flavors and the two Fanaroff-Riley structure classes.

1.3.3.4 Spectral index

The bases of weak-flavor jets exhibit a remarkably narrow range of initial spectral indices $\alpha \sim 0.62$, corresponding to a radiating particle energy index of 2.24, in the regions where the jets brighten before they flare. The spectral index α then decreases, both with increasing distance from the AGN and towards the edges of the jets, usually falling to $\alpha \sim 0.5$ to 0.55, before it eventually increases with distance from the AGN (as expected from synchrotron ageing). Strong-flavor jets have somewhat steeper spectra than those found at the bases of weak-flavor jets, with indices in the range $\alpha \sim 0.65$ to 0.9. Less is known about their internal spectral structure, due to generally poorer transverse resolution.

1.3.3.5 Proper motions

The FR I sources in which weak-flavor jets are found are thought to be the side-on counterparts of the BL Lac objects, in which pc-scale relativistic motion is well-established (Urry & Padovani, 1995). Superluminal motions have been seen directly on milliarcsecond scales in several weak-flavor jets (Giovannini *et al.*, 2001) and on arc-second (Biretta *et al.*, 1995) but *not* milliarcsecond (Kovalev *et al.*, 2007) scales in the M 87 jet. Knots in the closest known AGN jet, in Cen A (Hardcastle *et al.*, 2003) show proper motions at $\sim 0.5c$ in the brighter jet and are much brighter than any counterparts in the counterjet.

1.3.3.6 Arcs, knots, and filaments

Some weak-flavor jets are crossed by "arc"-like emission features in which the apparent magnetic field is tangent to the arc. The shapes of these arc-like features also exhibit systematic differences between the main and counterjets which can be

explained by differential relativistic aberration (Laing *et al.*, 2006c) .

Some strong-flavor jets (*e.g.*, Figure 1.5) exhibit semi-periodic strings of knots (Bridle *et al.*, 1994). Phenomena that could produce this include non-linear growth of Kelvin-Helmholtz instabilities, criss-crossing oblique shocks in confined jets, or regular perturbations of the flow velocity or direction at the AGN. High resolution imaging and polarimetry with EVLA or e-MERLIN will help us explore these phenomena more fully.
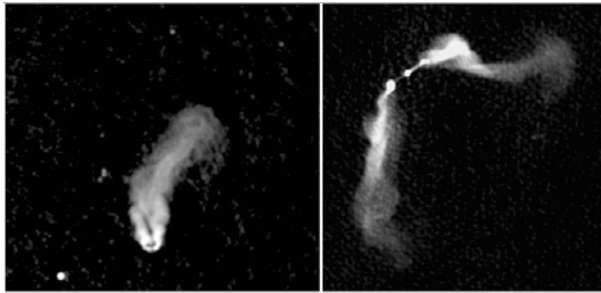
1.3.4
Jet bending on kpc scales

Figure 1.14 Bending of jets in cluster environments. Left: The Narrow-Angle-Tail source 3C 83.1 around NGC 1265 (VLA image at 1.4 GHz with 12″ FWHM resolution; the extended structure shown is ∼ 300 kpc in extent. Right: The Wide-Angle-Tail source 3C 465 around NGC 7720 (VLA image at 1.6 GHz with 5″ FWHM resolution; the extended structure shown is ∼ 360 kpc in extent.

Weak-flavor jets in dense environments can be bent into U-shapes by ram pressure of the "cross winds" resulting from movement of their parent galaxy relative to the cluster intergalactic gas, as in the "narrow angle tail" NGC 1265 (O'Dea & Owen, 1986). A second class of bent source appears to be bent by global flows from sub-cluster merger events (Loken *et al.*, 1995), as in "wide-angle tail" sources such as NGC 7720 (Figure 1.14). Numerical simulations by Balsara & Norman (1992) and lab experiments by Lebedev *et al.* (2004) imply that jet bending by a cross-wind proceeds by driving oblique shocks into the flow, producing a series of deflections by continual contact with the "wind". The jets in "wide-angle tails" (O'Donoghue *et al.*, 1993) initially resemble strong-flavor jets, i.e. they are straight, narrow and relatively inconspicuous until they suddenly brighten, bend, and broaden into the meandering plumes. The location of the strongest bending in these sources may mark the transition from jet propagation in the ISM of the galaxy into propagation in the global flow in the intra-cluster medium, but the mechanism of this transition is unclear (Loken *et al.*, 1995; Jetha *et al.*, 2005; Hardcastle *et al.*, 2005) because there is no clear X-ray evidence for discontinuities in the gas properties near the jet-plume transitions.

1.4
Modeling jet kinematics from radio data

The kinematics and magnetic field evolution of well-resolved weak-flavor jets can be inferred by fitting 3-d models of their geometry, velocity fields, emissivity variation and magnetic field anisotropies to sensitive radio imaging and polarimetry. The input data needed are deep, well-resolved images of Stokes parameters I, Q, and U at several frequencies. An essential requirement is to measure the percentage and intrinsic E-vector directions of the linear polarization (corrected for foreground Faraday rotation) throughout the jets and the counterjets in the same source. The apparent brightness ratios and the polarization asymmetries between the main jet and the counterjet are then used *simultaneously* to constrain fits of parameterized 3-d models to the data. The key assumption is that the jet and the counterjet are *intrinsically identical* axisymmetric outflows with relativistic velocities $v = \beta c$ and magnetic field anisotropies that vary both *across* (*i.e.*, transverse to the jets) and *along* them. The spreading geometry is determined from the observed jet shapes. The parameters decribing the flow velocity field, emissivity and magnetic field geometry are then adjusted to minimize residuals between the observed intensity and polarization data and the jet and counterjet models integrated through the jets at every measured position taking account of relativistic aberration and of the resolution of the telescope.

1.4.1
Intensity asymmetry modeling: velocity-angle degeneracy

The variations of the jet-counterjet brightness asymmetry (*i.e.*, of the jet "sidedness") along and across both jets are assumed to arise from the dependence of observed intensity $S_\nu = \delta^{(2+\alpha)} S_0(\nu)$ on the Doppler factor $\delta = 1/\Gamma(1 \pm \beta \cos \theta)$ and angle θ to the line of sight via relativistic beaming. As the observed sidedness ratios constrain only $\beta \cos \theta$, however, fits to sidedness alone are degenerate in β and θ. As described in §2.2, this degeneracy can be resolved for parsec-scale jets using constraints from the apparent superluminal motion. For kpc-scale weak-flavor jets it can be resolved by taking account of the *systematic* jet-counterjet polarization asymmetry.

1.4.2
Polarization asymmetry modeling: resolving the degeneracy

Differential relativistic aberration makes the *observed* inclination angles θ' to the line of sight $\sin \theta' = \delta \sin \theta$ systematically different throughout the jet and the counterjet. For well-resolved relativistic jets with anisotropic magnetic fields, the observed degree and orientation of the net linear polarization differ between the two jets in ways that depend on the variation of the ratios of the radial, toroidal and longitudinal field components along the lines of sight through the jets, and on the jet velocity fields. This dependence lets us solve for the magnetic field struc-

ture, velocity fields and orientation of well-resolved, polarized jets and counterjets simultaneously, removing the degeneracy between β and θ.
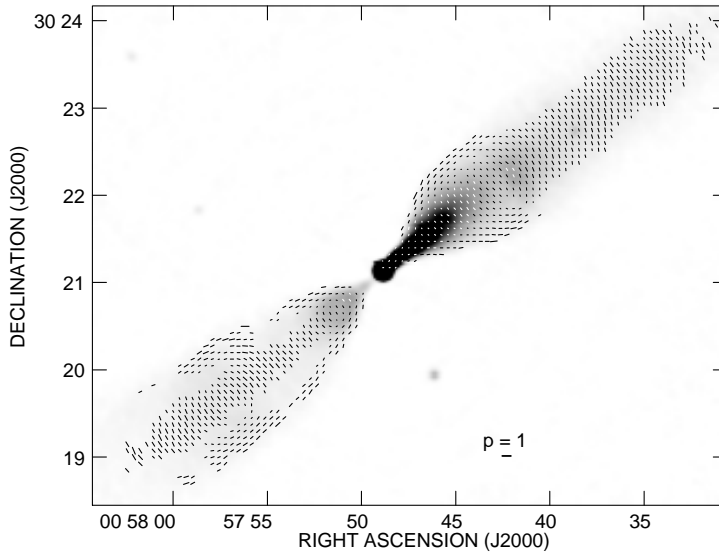

Figure 1.15 The magnetic field configuration in NGC315 at 5.5 ″ FWHM resolution. Lengths of vectors are proportional to the degree of linear polarization p and their orientations are those of the apparent magnetic field. Reproduced by permission of the Royal Astronomical Society.

Figure 1.15 shows the generic polarization structure *observed* in straight segments of weak-flavor jets just after the transition region: the apparent magnetic field is transverse to the jet near the jet axis but longitudinal near its edges (Figure 1.15). A 3-d ordered helical field can exhibit such a polarization pattern but well-ordered helical fields cannot reproduce the observed *transverse symmetry* of the total intensity and degree of polarization profiles (Laing *et al.*, 2006a). Figure 1.16 sketches two ways in which *anisotropic* field configurations with significant longitudinal and toroidal components *can* in principle produce the observed transverse profiles. The first configuration has a *spine* of two-dimensional field tangled in the plane perpendicular to the jet (with little longitudinal component) surrounded by a *sheath* of purely longitudinal field. Such a configuration might arise if a fast-moving jet spine is surrounded by a slower-moving boundary layer where velocity shear makes the perpendicular fields become longitudinal. The second configuration (Model 'B' of Laing (1980)) has concentric two-dimensional sheets of tangled longitudinal and toroidal field but little or no radial field, owing to velocity shear between the (fast)
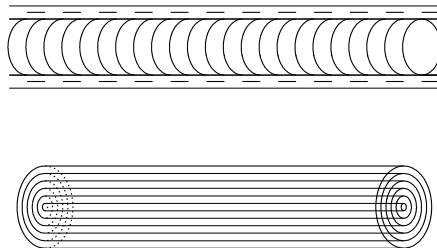
center and (slower) edges of the jet.

Figure 1.16 Two local geometries for tangled-magnetic-field configurations that might account for the generic polarization structure shown in Figure 1.15, ignoring the jet expansion for simplicity. (Upper) A "spine" in which the fields are tangled in the plane perpendicular to the jet axis, surrounded by a "sheath" dominated by longitudinal field - only sheath field is shown explicitly. (Lower) Sheets of tangled field with equal longitudinal and toroidal components wrapped around the jet axis. Only the concentric cylindrical geometry of the tangled field sheets is shown, not the tangled fields themselves.

Figure 1.17 shows how the two anisotropic field configurations shown in Fig. 1.16 can be distinguished in *decelerating* relativistic jets by the relative positions of the transition between apparently longitudinal and perpendicular fields on the axes of two intrinsically identical, conically expanding, jets. In the first case, this transition occurs further from the nucleus in the counterjet (and may not be seen at all in the main jet). In the second case, the converse is expected.

In *every* weak-flavor jet for which good data are available, the transition from parallel to perpendicular apparent field near the jet axis occurs further from the AGN in the brighter jet, *i.e.*, the actual 3-d field configuration must be a closer match to the *wrapped-sheet* case. Detailed modeling of individual jets using parameterized variants of this configuration can then be used to quantify how the field components vary with distance from the AGN in those jets, as illustrated in Figure 1.18.

1.4.3
Velocity fields in weak-flavor jets

Laing & Bridle (2002a) used an iterative procedure to fit (in the χ^2 sense) a parametric jet model to the correlated jet-counterjet brightness and polarization asymmetries in 3C 31 (Figure 1.2) and to derive how the flow velocity and field components evolve along this jet. Applying this approach to straight segments of other well-resolved weak-flavor jets (Canvin & Laing, 2004; Canvin *et al.*, 2005; Laing *et al.*, 2006c) has shown that their systematic asymmetries can be well accounted for if:
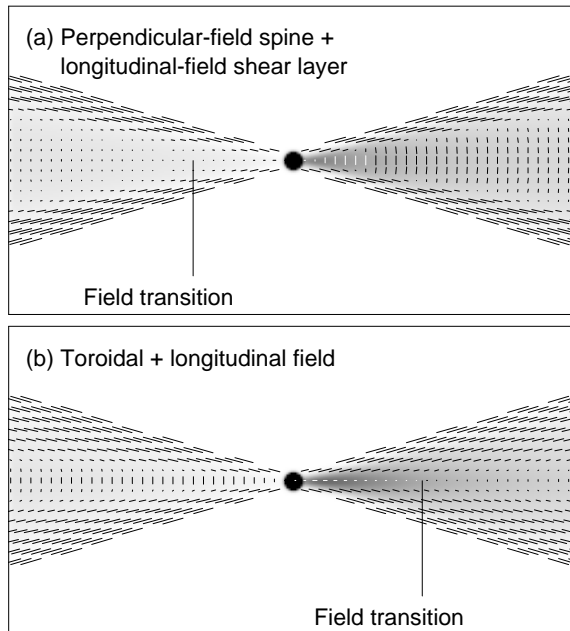
Figure 1.17 Examples of apparent magnetic field configurations resulting from two possible magnetic field configurations in a relativistic jet decelerating with the parameters inferred for NGC315 by Canvin *et al.* (2005). Lengths of vectors are proportional to the degree of linear polarization p and their orientations are those of the apparent magnetic field.

- β is about 0.8 to 0.9 where the jets first brighten
- All of the jets decelerate abruptly in the "flaring" region where they begin to spread rapidly, but the deceleration and flaring take place at different distances from the nucleus in different sources
- The jets decelerate to $\beta = 0.1$ to 0.4 further from the nucleus, sometimes achieving constant. low velocities before intrinsic asymmetries begin to dominate
- The outflow near the edges of many weak-flavor jets is slower than the outflow on-axis, so there is significant velocity shear across them, although some regions have a top-hat velocity profile

1.4.4
Magnetic field evolution in weak-flavor jets

The magnetic field configurations inferred from fitting observed jet-counterjet linear polarization distributions and their asymmetries determine field component *ratios*, not the absolute field strengths or topologies. Some clear systematics of the ratios in weak-flavor jets have emerged:
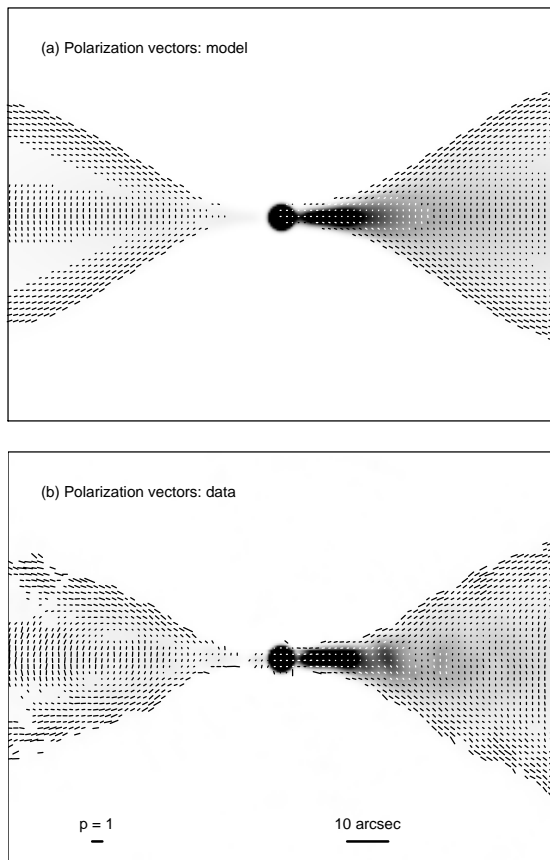
Figure 1.18 Observed and modeled polarization distributions for the inner jet and counterjet in the FR I radio galaxy NGC 315 (Canvin *et al.*, 2005). Lengths of vectors are proportional to the degree of linear polarization p and their orientations are those of the apparent magnetic field. Reproduced by permission of the Royal Astronomical Society.

- The longitudinal and toroidal components are generally similar to each other close to the nucleus, but the toroidal component dominates at large distances. This behavior is qualitatively, but not quantitatively, as expected from flux-freezing in an expanding flow wherein the longitudinal field component would be $\propto r_{\mathrm{jet}}^{-2}$ while the toroidal field component would be $\propto (\Gamma \beta r_{\mathrm{jet}})^{-1}$.
- The radial field components are generally weak compared to the other components. The jets in 3C 31, which show unusually clear evidence for ongoing deceleration at large distances from the AGN, also have unusually strong radial field components at their edges. This suggests a connection between ongoing deceleration of that jet and maintenance of some radial field by turbulent en-

trainment during ingestion of the ISM across its boundary. In other sources the radial field may be suppressed by the velocity shear.

We emphasize that these systematics are derived from studies of the initial segments of weak-flavor jets within which both the jet and counterjet remain sensibly straight and collinear. Far from the AGN, both the morphologies and magnetic field structures of the weak-flavor jets and their counterjets are modified by ongoing interactions with their environments, as evidenced by large-scale bending of the jets and the formation of plumes or lobes (figs.1.2,1.3,1.14).

1.4.5
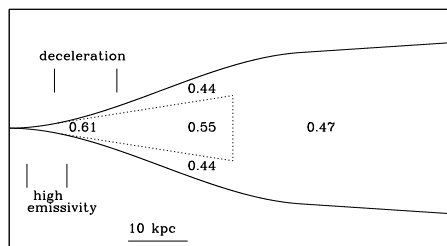## Emissivity evolution in weak-flavor jets

Figure 1.19 Jet deceleration, emissivity and spectral index (values shown) in the inner 80 kpc of the base of the jet in NGC 315. (Laing *et al.*, 2006b). Reproduced by permission of the Royal Astronomical Society.

Far from the AGN, where jet deceleration inferred from model fitting again becomes slow, the emissivities of weak-flavor jets decline with distance roughly *adiabatically*, *i.e.*, the rate of decline is consistent with flux-freezing with the observed spreading rate, and no particle acceleration. In the initial fast-moving and rapid-deceleration regions, there are *two* distinct regions where particle acceleration is required. The first is associated with enhanced X-ray emission and with the appearance of non-axisymmetric knots in the jets (*e.g.*, Worrall *et al.* (2007)). The second appears to be associated with velocity gradients (i.e. with velocity shear) at the jet edges.

- Jet brightening always begins shortly before the most rapid deceleration, which is in turn complete before recollimation occurs.
- The regions of high X-ray to radio brightness ratio are also regions of high flow velocity
- The initial energy index of 2.24 is close to that of 2.23 expected in the limit from Fermi I acceleration by ultra-relativistic shocks but the flow velocities inferred where this index occurs are less than expected from this interpretation.

Figure 1.19 sketches the relationship between regions of enhanced emissivity,

strongest jet deceleration, and spectral index structure at the base of the well-resolved jet in NGC 315 (Laing *et al.*, 2006b).

1.4.6
Mass, momentum and energy fluxes

Once the jet velocity field and spreading geometry are known, application of the relativistic conservation laws for mass, energy and momentum lets us deduce the global variations of density, pressure and entrainment rate along the jets when the confining media have been detected by X-ray observations. For such sources we can estimate the external pressure gradient within which the kinematics have been manifested, so we can obtain constraints on jet dynamical quantities. For 3C 31, Laing & Bridle (2002a) showed that well-constrained solutions exist subject to two key assumptions:

- $\Phi = \Pi c$ where Φ is the energy flux (with rest mass energy subtracted) and Π is the momentum flux. This must hold quite accurately if the jets have decelerated from bulk Lorentz factors on parsec scales.
- The jets reach pressure balance with the external medium in their outer regions, as suggested by their eventual recollimation.

Boundary-layer entrainment (*ingestion* of the ISM across the surface of the jets) and mass input (*injection*) from stars within the volume traversed by the jets are probably both important in slowing the weak-flavor jets in FR I sources. Conservation-law model fits (*e.g.*, Laing & Bridle (2002b)) suggest that the jets are initially light enough to be slowed significantly by stellar mass injection which may enable them to reach a transonic regime in which the ingestion of ambient ISM across the jet boundary is significant, as suggested by Bicknell (1995). For example, the internal Mach number inferred for 3C 31 by Laing & Bridle (2002b) was ≈ 1.5 through the deceleration region, the mechanical luminosity of the jet was estimated at 1.1×10^{37} W, its mass flux 5×10^{-4} solar masses/year, and the entrainment rate 10 kpc from the AGN to be 1.2×10^{10} kg.kpc^{-1} s^{-1}

1.4.7
Comparisons with strong-flavor jets

The only strong-flavor jets which have been well enough resolved to allow detailed modeling of their 3-d emissivity and field structures are those in 3C 353 (Swain *et al.*, 1998). Even there, full kinematic modeling along the lines used for weak-flavor jets has not yet been possible, owing to the difficulty of detecting the counterjets at all with good transverse resolution, let alone obtaining the sensitive counterjet polarimetry needed to apply these methods. There is some evidence however that the magnetic fields in the jets of 3C 353 are also dominated by their toroidal and longitudinal components (Swain *et al.*, 1998).

The association of strong-flavor jets with the formation of compact hot spots in the lobes of FR II sources suggests that they maintain higher Mach numbers

than weak-flavor jets to large distances from the AGN, and perhaps undergo less deceleration, consistent with preserving the jet collimation. Until counterjets can be detected and resolved in more FR II sources with strong-flavor jets, it will remain difficult to compare their properties directly with those inferred from modeling the deceleration of weak-flavor jets.

The prominent differences between strong flavor jets in radio galaxies and quasars probably arise from the systematic orientational difference between them, with the radio galaxy population closer to the plane of the sky than the quasars.

Figure 1.20 The central region of the FR I radio galaxy B2 0206+35 showing apparent structural *asymmetries* between the jet and counterjet that can be explained by *symmetric* backflow (VLA 4.9 GHz image, 0.35″ FWHM). The field of view is ∼ 80″, corresponding to ∼ 60 kpc.

1.5
Backflow in bi-lobed FR I sources?

In a few of the "lobed" FR I sources whose structure suggests that their jets may be propagating through lobe material, the brighter jets are isophotally narrower than the counterjets, *e.g.*, Figure 1.20. High-resolution imaging of two such sources, B2 0206+35 and B2 0755+37 (Bondi *et al.*, 2000) has shown that their counterjets contain features whose geometry matches that of the brighter "main" jets, but with brightness *minima* near the jet axis where the brighter jets have brightness maxima. Furthermore, the edges of these counterjets appear *brightness-enhanced* compared to the corresponding structure around the main jets, so that the counterjets appear wider at low resolution. No examples are known where the main jets are isophotally wider than the counterjets. The brightness and polarization asymmetries

in these sources can be fitted with intrinsically symmetric relativistic jet models if both jets are surrounded by mildly relativistic symmetric *backflow*, which appears brighter around the counterjets and fainter around the edges of the main jets due to differential beaming (the backflow around the counterjet is *approaching* the observer, while that around the main jet is receding).

Such symmetric backflow has also been seen in some numerical simulations of over-pressured, fast, light jets (where it may however be an artifact of forced axisymmetry, low resolution, or open boundary conditions). Symmetric backflow might be thought hard to set up in practise, but the radio data suggest that it may, nevertheless, occur with $\beta \sim 0.05$ to 0.4 and enhanced emissivity in both B2 0206+35 and B2 0755+37. The dominant magnetic field component inferred in the putative backflow in these sources is, perhaps unsurprisingly (*e.g.*, Begelman, Blandford & Rees (1984)), toroidal. Whether such toroidal field (and associated return currents) in the backflow play a role in confining these jets is unclear because, as emphasized earlier, the field *strengths* are unknown without further assumptions.

1.6
Acknowledgments

References

Abraham, Z. & Romero, G.E. 1999, *A.& A.*, , 344, 61.

Agudo, I., *et al.* 2001, *Ap.J.*, 549, L183.

Agudo, I., *et al.* 2007, *A.& A.*, 476, L17.

Agudo, I. 2009, in *Approaching Micro-Arcsecond Resolution with VSOP-2: Astrophysics and Technology*, ASP Conference Series 402, eds. Y. Hagiwara, E. Fomalont, M. Tsuboi, and Y. Murata, 402, 330.

Balsara, D., & Norman, M. 1992, *Ap.J.*, 393, 631.

Beasley, A.J., Gordon, D., Peck, A.B., Petrov, L., MacMillan, D.S., Fomalont, E.B. & Ma, C. 2002, *Ap.J.Supp.*, 141, 13.

Begelman, M.C., Blandford, R.D., & Rees,M.J. 1984, Revs. Mod. Phys., 56, 255.

Bicknell, G.V. 1995, *Ap.J.Suppl.* 101, 29.

Biretta, J.A., Zhou, F., & Owen, F.N. 1995, *Ap.J.*, 447, 582.

Blandford, R.D. & Königl, A. 1979, *Ap.J.*, , 232, 34.

Bondi M., Parma P., de Ruiter H.R., Laing R.A., & Fomalont E.B. 2000, *M.N.R.A.S.*, 314, 11.

Bridle, A.H. 1984, *A.J.*, 89, 979.

Bridle, A.H. 1986, *Can.J.Phys.*, 64, 353.

Bridle, A.H. 1991, in *Testing the AGN Paradigm*, eds. S.S.Holt, S.G.Neff, & C.M.Urry, AIP Conference Proceedings 254, 386.

Bridle, A.H., Hough, D.H., Lonsdale, C.J., Burns, J.O., & Laing, R.A. 1994, *A.J.*, 108, 766.

Britzen *et al.* 2007, *A.& A.*, 472, 763.

Britzen *et al.* 2008, *A.& A.*, 84, 119.

Britzen *et al.* 2010, *A.& A.*, 515, 105.

Canvin, J.R. & Laing, R.A. 2004, *M.N.R.A.S.*, 350, 1342.

Canvin, J.R., Laing, R.A., Bridle, A.H., & Cotton, W.D. 2005, *M.N.R.A.S.*, 363, 1223.

Cara, A. & Lister, M.L. 2008, *Ap.J.*, 674, 111.

Carilli, C.L., Perley, R.A., Bartel, N., & Dreher, J.W. 1996, in *Cygnus A - Study of a Radio Galaxy*, eds. C.L.Carilli & D.E.Harris, Cambridge University Press, 76.

Chiaberge, M., Celotti, A., Capetti, A. & Ghisellini, G. 2000, *A.& A.*, 358, 104.

Cohen, M.H., Lister, M.L., Homan, D.C., Kadler, M., Kellermann, K.I., Kovalev, Y.Y. & Vermeulen, R.C. 2007, *Ap.J.*, 658, 232.

Conway, J.E. & Murphy, D.W. 1993, *Ap.J.*, , 411, 89.

Davis, R.J., Unwin, S.C. & Muxlow, T.W.B. 1991, *Nature*, 354, 374.

Denn, G.R., Mutel, R.L. & Marscher, A.P. 2000, *Ap.J.Supp.*, 129, 61.

Dodson, R. *et al.* 2008, *Ap.J.Supp.*, 175, 314.

Fanaroff, B.L., & Riley, J.M. 1974, *M.N.R.A.S.*, 167, 31P.

Fey, A.L., Clegg, A.W. & Fomalont, E.B. 1997a, *Ap.J.Supp.*, 105, 299.

Fey, A.L. & Charlot, P. 1997b, *Ap.J.Supp.*, 111, 95

Fey, A.L. & Charlot, P. 2000, *Ap.J.Supp.*, 128, 17.

Garrington, S.T., Conway, R.G., & Leahy, J.P. 1991, *M.N.R.A.S.*, 250, 171.

Garrington, S.T., Leahy, J.P., Conway, R.G., & Laing, R.A. 1988, *Nature*, 341, 147.

Giovannini G., Cotton W.D., Feretti L., Lara L., & Venturi T. 2001, *Ap.J.,* , 552, 508.

Giovannini, G., Cotton, W.D., Lara, L., Marcaide, J., & Wehrle, A.E. 1994, in *Compact Extragalactic Radio Sources*, eds. J.A.Zensus & K.I.Kellermann, NRAO, 61.

Hardcastle, M.J., Worrall, D.M., Kraft, R.P.,

Forman, W.R., Jones, C., and Murray, S.A. 2003, *Ap.J.*, 593, 169.

Hardcastle, M.J., Sakelliou, & Worrall, D.M. 2005, *M.N.R.A.S.*, 359, 1007.

Hardee, P.E., Walker, R.C. & Gomez, J.L. 2005, *Ap.J.*, , 620, 646.

Helmboldt, J. F. *et al.*, 2007, *Ap.J.*, 658, 203.

Homan, D.C., Lister, M.L., Kellermann, K.I., Cohen, M.H., Ros, E., Zensus, J.A., Kadler, M., and Vermeulen, R.C. 2003, *Ap.J.*, 589, L9.

Homan, D.C., Kovalev, Y.Y., Lister, M.L., Ros, E., Kellermann, K.I., Cohen, M.H., Vermeulen, R.C., Zensus, J.A. & Kadler, M. 2006, *Ap.J.*, 642, L115.

Horiuchi, S., Meier, D.L., Preston, R.A. & Tingay, S.J. 2006, PASJ, 58, 211.

Hough, D.H. *et al.* 2002, *A.J.*, 123, 1258.

Hough D. 2008, in *Extragalactic Jets: Theory and Observation from Radio to Gamma Ray*, ASP Conference Series, eds T.A. Rector and D.S. De Young, 386, 274.

Jetha, M.N., Sakelliou, I., Hardcastle, M.N., Ponman, T.J., & Stevens, J.R. 2005, *M.N.R.A.S.*, 358, 1394 **check**.

Jorstad, S.G. *et al.* 2005, *A.J.*, 130, 1418.

Kadler, M., Ros, E., Lobanov, A.P., Falcke, H. & Zensus, J.A. 2004, *A.& A.*, 426, 481.

Kellermann, K.I. & Pauliny-Toth, I.I.K. 1969, *Ap.J.*, 155, L71.

Kellermann, K.I., Vermeulen, R.C., Zensus, J.A. & Cohen, M.H. 1998, *A.J.*, 115, 1295.

Kellermann, K.I. *et al.* 2004, *Ap.J.*, 609, 539.

Kharb, P., Lister, M.L. & Cooper, N.J. 2010, *Ap.J.*, , 710, 764.

Königl, A. 1981, *Ap.J.*, , 243, 700.

Kovalev, Y.Y. *et al.* 2005,

Kovalev, Y.Y., Lister, M.L., Homan, D.C., & Kellermann, K.I. 2007, *Ap.J.*, 668, L27.

Kunert-Bajraszewska, M., Janiuk, A., Gawroński, M.P., & Siemiginowska, A. 2010, *Ap.J.*, 718, 1345.

Krichbaum, T.P., *et al.* 2007, in *Extragalactic Jets: Theory and Observation from Radio to Gamma Ray*, ASP Conference Series, eds T.A. Rector and D.S. De Young, 386, 186.

Lähteenmäki, A. & Valtaoja, E. 1999, *Ap.J.*, 521, 493.

Laing, R.A. 1980, *M.N.R.A.S.*, 193, 439.

Laing, R.A. 1988, *Nature*, 331, 149.

Laing, R.A. 1993, in *Astrophysical Jets*, eds. D.Burgarella, M. Livio, & C.P.O'Dea,

Astrophysics and Space Science Library, 103, 95.

Laing, R.A. 1996, in *Energy Transport in Radio Galaxies and Quasars*, eds. P.E.Hardee, A.H.Bridle, & J.A.Zensus, *A.S.P. Conf. Series* 100, 241.

Laing, R.A. & Bridle, A.H. 2002a, *M.N.R.A.S.*, 336, 328.

Laing, R.A. & Bridle, A.H. 2002b, *M.N.R.A.S.*, 336, 1161.

Laing, R.A., Canvin, J., & Bridle, A.H., 2006a, *Astron. Nacht.* 327, 523.

Laing, R.A., Canvin, J., Bridle, A.H., & Hardcastle, M.J. 2006c, *M.N.R.A.S.*, 372, 510.

Laing, R.A., Canvin, J., Cotton, W.D., & Bridle, A.H., 2006b, *M.N.R.A.S.*, 368, 48.

Laing, R.A., Parma, P., de Ruiter, H.R., & Fanti, R. 1999, *M.N.R.A.S.*, 306, 513.

Leahy, J.P. 1993, in *Jets in Extragalactic Radio Sources*, eds. H.-J. Röser & K. Meisenheimer, Lecture Notes in Physics, Berlin: Springer-Verlag 421, 1.

Lebedev, S. V., Ampleford, D., Ciardi, A., Bland, S. N., Chittenden, J. P., Haines, M. G., Frank, A., Blackman, E. G., & Cunningham, A. 2004, *Ap.J.*, 616, 988

Ledlow, M.J. & Owen, F.N. 1996, *A.J.*, 112, 9.

Lee, S.S. *et al.* 2008, *A.J.*, 136, 159.

Lind, K.R. & Blandford, R.D. 1985, *Ap.J.*, 295, 358.

Lister, M.L. & Marscher, A.P. 1997, *Ap.J.*, 476, 572.

Lister, M.L. *et al.* 2009a, *A.J.*, 137, 3718.

Lister, M.L. *et al.* 2009b, *A.J.*, 138, 1874.

Lobanov, A. & Zensus, A. 2003, Science, 294, 128.

Lobanov, A.P. 1989, *A.& A.*, 330, 79.

Loken, C., Roettiger, K., Burns, J.O., & Norman, M. 1995, *Ap.J.* 445, 80.

Ly, C., Walker, R.C. & Junor, W. 2007, *Ap.J.*, , 660, 200.

Marscher, A.P., 2008, in *Extragalactic Jets: Theory and Observation from Radio to Gamma Ray*, ASP Conference Series, eds T.A. Rector and D.S. De Young, 386, 437.

Moellenbrock, G.A. *et al.* 1996, A.J., 111, 2174.

Morganti, R., Parma, P., Capetti, A., Fanti, R., & de Ruiter H.R. 1997, *Astron.Astrophys.*, 326, 919.

O'Dea, C.P. 1998, *PASP*, 110, 493.

O'Dea, C.P., & Owen, F.N. 1986, *Ap.J.*, 301,

841.

O'Donoghue, A., Eilek, J.A., & Owen, F.N. 1993, *Ap.J.*, 408, 428.

Ojha, R. *et al.* 2010, *A.& A.*, , 519, 450.

Orienti, M. & Dallacasa, D. 2010, *M.N.R.A.S.*, , 406, 529.

O'Sullivan, S.P. & Gabuzda, D.C. 2009, *M.N.R.A.S.*, , 400, 26.

Owen, F.N. & White, R.A. 1991, *M.N.R.A.S.*, 249, 164.

Parma, P., de Ruiter, H.R., & Fanti, R. 1996, in *Extragalactic Radio Sources*, eds. R.Ekers, C.Fanti, & L.Padrielli, *I.A.U. Symp. 175*, 137.

Pearson, T.J. & Readhead, A.C.S. 1988, *Ap.J.*, 328, 114.

Piner, B.G., Mahmud, M., Fey, A.L. & Gospodinova, K. 2007, *A.J.*, 133, 2357.

Readhead, A.C.S. 1994, *Ap.J.*, 426, 51.

Roca-Sogorb, M,. Gomez, J.L., Agudo, I., Marscher, A.P. & Jorstad, S.G. 2010, *Ap.J.*, 712, L160.

Scheuer, P.A.G & Readhead, A.C.S. 1979, *Nature*, 277, 182.

Swain, M.R., Bridle, A.H., & Baum, S.A. 1998, *Ap.J.Letters*,

Taylor, G.B., Vermeulen, R.C., Readhead, A.C.S., Pearson, T.J., Henstock, D.R. & Wilkinson, P.N. 1996, *Ap.J.Supp.*, 107, 37-68.

Urry, C.M., & Padovani, P. 1995, *PASP*, 107, 803.

Venturi, T., Castaldini, C., Cotton, W.D., Feretti, L., Giovannini, G., Lara, L., Marcaide, J.M., & Wehrle, A.E. 1995, *Ap.J.*, 454, 735.

Venturi, T., Giovannini, G. Feretti, L., Cotton, W.D., Lara, L., Marcaide, J., & Wehrle, A. 1994, in *The Physics of Active Galaxies*, eds. G.V.Bicknell, M.A.Dopita, & P.J.Quinn, *ASP Conference Series* 54, 241.

Vermeulen, R.C., Ros, E., Kellermann, K.I., Cohen, M.H., Zensus, J.A. and van Langevelde, H.J. 2003, *A.& A.*, 401, 113.

Vermeulen, R.C. and Cohen, M.H. 1994, *Ap.J.*, 430, 467.

Walker, R.C., Dhawan, V., Romney, J.D., Kellermann, K.I. & Vermeulen, R.C. 2000, *Ap.J.*, 530, 233.

Worrall, D.M., Birkinshaw, M., Laing, R.A., Cotton, W.D., & Bridle, A.H. 2007, *M.N.R.A.S.*, 380, 2.